


# Astrometry and infrared observations of the Mira variable stars AP Lyncis, V837 Herculis, and BX Camelopardalis: Implications for the period–luminosity relation of the Milky Way

James O. CHIBUEZE <sup>1,2,\*</sup>, Riku URAGO,<sup>3</sup> Toshihiro OMODAKA,<sup>3</sup>  
Yuto MORIKAWA,<sup>3</sup> Masayuki Y. FUJIMOTO,<sup>4</sup> Akiharu NAKAGAWA,<sup>3</sup>  
Takahiro NAGAYAMA,<sup>3</sup> Takumi NAGAYAMA,<sup>5</sup> and Ken HIRANO<sup>5</sup>

<sup>1</sup>Centre for Space Research, Physics Department, North-West University, Potchefstroom 2520, South Africa.

<sup>2</sup>Department of Physics and Astronomy, Faculty of Physical Sciences, University of Nigeria, Carver Building, 1 University Road, Nsukka, Nigeria

<sup>3</sup>Department of Physics and Astronomy, Graduate School of Science and Engineering, Kagoshima University, 1-21-35 Korimoto, Kagoshima, Kagoshima 890-0065, Japan

<sup>4</sup>Department of Physics, Hokkaido University, Sapporo, Hokkaido 060-0810, Japan

<sup>5</sup>Mizusawa VLBI Observatory, National Astronomical Observatory of Japan, 2-21-1 Osawa, Mitaka, Tokyo 181-8588, Japan

\*E-mail: [james.chibueze@unn.edu.ng](mailto:james.chibueze@unn.edu.ng)

Received 2020 March 3; Accepted 2020 May 24

## Abstract

AP Lyn and V837 Her are long-period Mira variable stars in the Milky Way. We performed VLBI Exploration of Radio Astrometry (VERA) phase-referenced observations towards H<sub>2</sub>O masers associated with AP Lyn and V837 Her. The annual parallaxes of AP Lyn and V837 Her were obtained to be  $2.008 \pm 0.038$  mas and  $1.090 \pm 0.014$  mas, corresponding to distances of  $498 \pm 10$  pc and  $917 \pm 12$  pc, respectively. From our multi-epoch infrared observations using the Kagoshima University 1 m telescope, we derived the mean *J*-, *H*-, and *K*-band magnitudes of AP Lyn, V837 Her, and an additional long-period Mira variable BX Cam, whose parallax is known. We derived their pulsation periods to be  $433 \pm 1$  d,  $520 \pm 1$  d, and  $458 \pm 1$  d, respectively, using the *K*-band light curves. The  $M_K$ –log *P* relation of long-period Mira variables seem to be violated by Mira variable stars with larger-than-expected  $M_K$  values (like OZ Gem) in the Milky Way because of circumstellar extinction leading to an observed dimming effect. AP Lyn, V837 Her, and BX Cam (like OZ Gem) are dimming from the trend to O-rich stars in the Large Magellanic Cloud. This implies that the high metallicity of the Milky Way galaxy increases the opacity of the Mira-type variable stars and strengthens mass loss.

**Key words:** astrometry — masers (H<sub>2</sub>O) — stars: AGB and post-AGB — stars: individual (AP Lyncis, V837 Herculis, BX Camelopardalis)

## 1 Introduction

Long-period ( $\log P > 2$ ) Mira variables (LPVs) with large amplitudes ( $\delta V > 2.5$  mag) are essential for the construction of the period–luminosity relation of late-type stars in a galaxy. Among the plethora of complex processes involved in the asymptotic giant branch (AGB) phase, stellar pulsation is one of the most interesting. Stellar pulsation is related to poorly understood processes such as mass loss and dust formation, and it is also an extremely valuable observable for the testing of theoretical models. It can also be used to estimate global stellar parameters, because pulsation periods are strongly linked to stellar mass, radius, and effective temperature.

The relationship between the  $K'$ -band absolute magnitude ( $M_K$ ) and the logarithm of the pulsation period ( $\log P$ ) of Mira variables are well constrained for the Large Magellanic Cloud (LMC; Feast et al. 1989; Ita et al. 2004), and serve as distance indicator. The  $M_K$ – $\log P$  relation of the LMC may not be adopted for the Milky Way because the metallicity of the Milky Way is twice that of the LMC (Luck et al. 1998), thus we need to derive the  $M_K$ – $\log P$  relation peculiar to the Milky Way. This task can be daunting considering the high uncertainties in their distance estimates, which introduces significant errors in the  $M_K$  values. Deriving the accurate distances to AGB stars with very-long-baseline interferometry (VLBI) astrometric techniques is one way to constrain the  $M_K$ – $\log P$  relation of the Milky Way and compare it to that of the LMC. It is important to note that the pulsation period of a Mira variable star is independent of the wavelength at which it is measured; however, the accuracy of the measurement depends on the number of cycles covered and the observation cadence.

Like long-period Mira variables, OH/IR stars also have long pulsation periods (500–1800 d) and undergo mass loss. They are known to be associated with OH masers and bright in the infrared wavelengths (Engels et al. 1983). Many OH/IR star candidates have been found in the Milky Way, but only a few are known in the LMC and Small Magellanic Cloud (Goldman et al. 2018). The position of OH/IR stars on the  $M_K$ – $\log P$  relation could be a reflection of the evolutionary differences between galaxies. The most popular  $M_K$ – $\log P$  relation is that of the LMC (Feast et al. 1989). The zero point of this relation has been applied to derive the  $M_K$ – $\log P$  relation of Galactic Mira variable stars (Whitelock et al. 2000; Knapp et al. 2003). The dependence of the  $M_K$ – $\log P$  relation on the metallicity of the galaxy could mean that merely adapting the LMC relation for the Milky Way or other galaxies could be misleading, as in the case of OZ Gemini (hereafter OZ Gem). Urago et al. (2020b) confirmed OZ Gem as the first Mira variable star at

the same position as OH/IR stars on the  $M_K$ – $\log P$  relation in the Milky Way. They suggested that circumstellar dust around OZ Gem caused it to have a larger value of  $M_K$  than expected. OZ Gem, which has been confirmed as an O-rich star by spectroscopy, falls in the area occupied by C-rich stars on the  $M_K$ – $\log P$  relation of the LMC. OZ Gem is in the thermally pulsing AGB (TP-AGB) evolution stage, either without experiencing the third dredge-up (TDU) or truncated before becoming a C-rich star via TDU, attributable to the high metallicity of the Milky Way. Is OZ Gem just an isolated unique case? Are there other OZ Gem-like Mira variables in the Milky Way? Answers to the above questions could revolutionize our understanding of the  $M_K$ – $\log P$  relation and, by extension, the period–luminosity relation of the Milky Way.

AP Lyn (hereafter AP Lyn; also known as IRC +60169 or IRAS 06300+6058) and V837 Her (also known as IRC +10374 or IRAS 18413+1354) are both M7 stars (Vogt 1973; Stephenson 1986). Both have been confirmed to be associated with H<sub>2</sub>O, SiO  $v = 1$  and  $v = 2$  transitions (Kim et al. 2014), and OH maser emission (Engels & Bunzel 2015). BX Camelopardalis (hereafter BX Cam; also known as IRC +70066) is an M9.5 star with a  $G$ -band magnitude of 8.839 mag and an effective temperature of 3292.25 K (Gaia Collaboration 2018). Gaia Data Release 2 (DR2) reported the  $G$ -band mean magnitude of AP Lyn and V837 Her to be 8.8321 mag and 10.5485 mag with effective temperatures of  $T_{\text{eff}} = 3281.33$  K and 3283 K (Gaia Collaboration 2018), respectively. They also estimated the parallaxes to be  $1.96 \pm 0.23$  mas (a distance of  $510^{+68}_{-54}$  pc) for AP Lyn and  $1.41 \pm 0.25$  mas ( $710^{+150}_{-110}$  pc) for V837 Her. The distance to AP Lyn was reported as 177 pc using spectral types and visual flux (Celis 1995). In contrast, the distance of V837 Her was derived as 2.93 kpc using the radial velocity and Oort's galactic rotation model for a zero-point calibration in the distance modulus (Yuasa et al. 1999). Matsuno et al. (2020) reported the parallax of BX Cam to be  $1.73 \pm 0.03$  mas, corresponding to a distance of  $578 \pm 10$  pc. We have adopted this distance for BX Cam throughout this paper. AP Lyn, V837 Her, and BX Cam are long-period Mira variable stars.

In this paper we report the results of the VERA trigonometric annual parallax measurement of the H<sub>2</sub>O masers associated with AP Lyn and V837 Her. With the BX Cam parallax measurement from (Matsuno et al. 2020), we included the target in our discussions of the  $M_K$ – $\log P$  relation. This paper also contains the results of our multi-epoch infrared observations of AP Lyn, V837 Her, and BX Cam, and a comparison on the  $M_K$ – $\log P$  relation plane with the results of OZ Gem (Urago et al. 2020b) and those of the LMC (e.g., Ita & Matsunaga 2011).

**Table 1.** VLBI observations of AP Lyn.<sup>†</sup>

No	Date yyyy mm dd	$T_{\text{sys}}$ (K)			
		MIZ	IRK	OGA	ISG
*	2005 02 22	190	180	230	320
*	2005 03 26	290	230	210	520
*	2005 04 23	140	190	310	1360
*	2005 05 22	200	410	380	480
1	2006 10 28	190	200	790	340
2	2006 11 26	370	440	450	670
3	2007 01 05	110	150	210	230
4	2007 02 09	160	430	160	1010
5	2007 03 16	120	550	810	290
6	2007 04 08	250	150	240	850
7	2007 05 05	220	1220	210	500
8	2007 09 08	330	250	380	4260

<sup>†</sup>Column 1 lists the number of the observation epoch. “\*” were not used for the parallax measurement (see subsection 2.1). Column 2 lists the date of the observation. Columns 3 to 6 list the system noise temperatures of the four VERA antennas at Mizusawa (MIZ), Iriki (IRK), Ogasawara (OGA), and Ishigaki-jima (ISG).

**Table 2.** VLBI observations of V837 Her.<sup>†</sup>

No	Date yyyy mm dd	$T_{\text{sys}}$ (K)			
		MIZ	IRK	OGA	ISG
1	2009 10 25	140	790	350	270
2	2010 01 10	120	170	160	250
3	2010 04 02	120	120	220	450
*	2010 08 17	380	440	380	430
4	2010 11 04	220	130	400	450
5	2011 01 15	100	110	160	310
6	2011 04 08	—	190	170	270
*	2011 08 18	980	500	380	310
7	2011 11 20	160	120	340	260

<sup>†</sup>Column 1 lists the number of the observation epoch. “\*” were not used for the parallax measurement (see subsection 2.1). Column 2 lists the date of the observation. Columns 3 to 6 list the system noise temperatures of the four VERA antennas at Mizusawa (MIZ), Iriki (IRK), Ogasawara (OGA), and Ishigaki-jima (ISG).

## 2 Observations and data reduction

### 2.1 VERA observations

VLBI observations of 22.235080 GHz  $\text{H}_2\text{O}$  masers in AP Lyn and V837 Her were made with VERA. The observation dates of AP Lyn and V837 Her are summarized in tables 1 and 2, respectively. The system noise temperatures of the four VERA antennas at Mizusawa (MIZ), Iriki (IRK), Ogasawara (OGA), and Ishigaki-jima (ISG) are also summarized. AP Lyn was observed over 12 epochs between 2005 and 2007. For four epochs in 2005, the  $\text{H}_2\text{O}$  maser of AP Lyn could not be detected because of the maser time variability. We used eight epochs between 2006 and 2007 for the parallax measurement. V837 Her was observed over

**Table 3.** Source list.\*

Source	RA (J2000.0)	Dec (J2000.0)
AP Lyn	06 <sup>h</sup> 34 <sup>m</sup> 33 <sup>s</sup> .4044	+60°56′27″.641
J0638+5933	06 <sup>h</sup> 38 <sup>m</sup> 02 <sup>s</sup> .871931	+59°33′22″.21467
V837 Her	18 <sup>h</sup> 43 <sup>m</sup> 36 <sup>s</sup> .4603	+13°57′22″.744
J1844+1312	18 <sup>h</sup> 44 <sup>m</sup> 07 <sup>s</sup> .262587	+13°12′28″.03911

\*Column 1 lists the source name. Columns 2 and 3 list the delay tracking center in RA and Dec, respectively.

nine epochs between 2009 and 2011. For two epochs, 2010 August 17 and 18, the maser of V837 Her could not be detected because of the high system noise temperatures caused by bad weather conditions. The remaining seven epochs were used for the parallax measurement. The observation on 2011 April 8 was done with just the IRK, OGA, and ISG antennas, as the MIZ antenna was unavailable.

The target maser and the position reference continuum source were simultaneously observed with the dual-beam system of VERA. The position reference source of AP Lyn is J0638+5933 and the separation angle is 1°.45. The position reference source of V837 Her is J1844+1312 and the separation angle is 0°.76. These two reference sources are listed in the second realization of the International Celestial Reference Frame (ICRF2) catalog (Fey et al. 2004). The source coordinates used for the delay tracking centers are listed in table 3. The received signals were recorded using a Sony DIR 2000 system with a recording rate of 1 Gbps with 16 video channels of 16 MHz bandwidth. One channel was assigned to the target maser source and the other 15 channels were assigned to the position reference source. Correlation processes were carried out using the Mitaka FX correlator. The frequency spacing for the maser source is 31.25 kHz, corresponding to a velocity of 0.42 km s<sup>-1</sup>.

We used the NRAO AIPS package for the phase-referencing data calibration and the imaging. The amplitude calibration was performed using the system noise temperatures during the observations. For phase-referencing, fringe fitting was performed using the AIPS task FRING on J0638+5933 and J1844+1312. The solutions were applied to the data of V837 Her and AP Lyn to calibrate the visibility data. The phase solutions obtained from the self-calibration of J0638+5933 and J1844+1312 were also applied to AP Lyn and V837 Her. Figure 1 shows the self-calibration maps. J0636+5933 and J1844+1312 were detected at peak intensities of  $\sim 300$  mJy beam<sup>-1</sup> and  $\sim 80$  mJy beam<sup>-1</sup>, respectively. J0636+5933 has a structure that is elongated in the northeast–southwest direction. This structure is also seen in VLBA images at 22 GHz and 43 GHz (Orienti et al. 2006). J1844+1312 is point-like, indicating a good source for phase-referencing. The instrumental phase difference between the two beams was

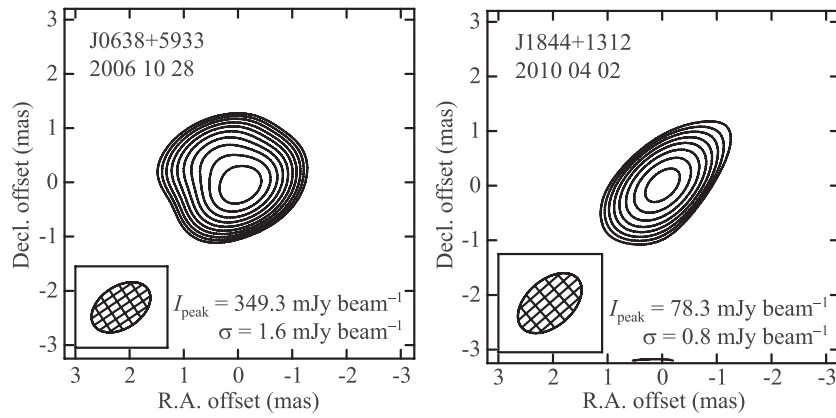


**Fig. 1.** Self-calibration maps of the position reference sources, J0638+5933 (left) and J1844+1312 (right). The peak intensity ( $I_{\text{peak}}$ ) and the noise level ( $\sigma$ ) are shown in the bottom corner in each panel. The contour levels are  $\sigma \times 5 \times \sqrt{2^n}$  ( $n = 1, 2, 3, \dots$ ).

measured continuously during the observations by injecting artificial noise sources into both beams (Honma et al. 2008a). The tropospheric delay was calibrated based on GPS measurements at the zenith delay (Honma et al. 2008b). After the calibration, we made spectral-line image cubes of the target maser sources using the AIPS task IMAGR. The emission peak was sought in the image field of  $1'' \times 1''$ . For each peak, the phase-referenced image with  $2048 \times 2048$  pixels and a pixel size of 0.05 mas was made with the CLEAN processing. The peak intensity and position were obtained by fitting a two-dimensional Gaussian to the emission on the image using the AIPS task IMFIT. A signal-to-noise ratio of  $\geq 7$  was adopted as the detection criterion for a maser spot. The noise levels of AP Lyn and V837 Her were  $0.1\text{--}0.2 \text{ Jy beam}^{-1}$  and  $0.2\text{--}0.3 \text{ Jy beam}^{-1}$ , respectively.

## 2.2 Near-infrared monitoring observations

For three target stars, V837 Her, AP Lyn, and BX Cam, we carried out near-infrared (NIR) observations from 2004 May to 2016 August using the Kagoshima University 1 m telescope. The near-infrared camera attached to the telescope has a  $512 \times 512$  pixel HAWAII array, which provides the  $J$ -,  $H$ -, and  $K'$ -band images. The image scale of the array is 0.636 pixel, yielding a field of view of  $5'.025 \times 5'.025$ . The data reduction and photometry for these data were carried out using the National Optical Astronomy Observatory Imaging Reduction and Facility (IRAF) software package. Standard procedures of data reduction were adopted. The average dark frame was subtracted, normalizing each of the dark-subtracted images by the flat-field frame. Subsequently, the sky frame was subtracted from the normalized image. The photometry was carried out with the IRAF/APPHOT package. Since these stars are too bright in the near-infrared, which causes saturation of the detector,

**Table 4.** Near-infrared photometry results of AP Lyn.

MJD	$m_J$ (mag)	$m_H$ (mag)	$m_{K'}$ (mag)	Remark
53365	$2.81 \pm 0.09$	$1.73 \pm 0.04$	–	defocus
53407	$2.01 \pm 0.03$	$1.14 \pm 0.02$	$0.42 \pm 0.06$	defocus
53436	$2.02 \pm 0.01$	$1.05 \pm 0.03$	–	defocus
53449	$1.53 \pm 0.42$	–	$0.39 \pm 0.07$	defocus
53469	$1.90 \pm 0.02$	$0.93 \pm 0.01$	$0.33 \pm 0.01$	defocus
53475	–	–	$0.33 \pm 0.03$	defocus
53495	$1.43 \pm 0.62$	–	$0.19 \pm 0.05$	defocus
54228	$2.85 \pm 0.01$	$1.71 \pm 0.02$	$0.92 \pm 0.03$	defocus
54419	$2.08 \pm 0.03$	$0.93 \pm 0.03$	–	defocus
54510	–	–	$0.80 \pm 0.04$	defocus
54528	–	–	$0.92 \pm 0.02$	defocus
54577	$3.40 \pm 0.05$	–	$0.98 \pm 0.02$	defocus
54816	$1.89 \pm 0.05$	–	$0.03 \pm 0.05$	defocus
54819	–	–	$0.09 \pm 0.07$	defocus
54870	$2.05 \pm 0.06$	$0.91 \pm 0.04$	–	defocus
54950	–	–	$0.87 \pm 0.03$	defocus
55092	$2.62 \pm 0.04$	$1.55 \pm 0.03$	$0.70 \pm 0.03$	defocus
55159	$1.05 \pm 0.49$	–	–	defocus
55804	$2.71 \pm 0.05$	$1.42 \pm 0.01$	–	defocus
55986	$4.48 \pm 0.06$	–	–	defocus
57026	–	–	$0.26 \pm 0.05$	LAF
57047	–	–	$0.37 \pm 0.05$	LAF
57330	–	–	$0.44 \pm 0.05$	LAF
57453	–	–	$0.38 \pm 0.05$	LAF
57510	–	–	$0.59 \pm 0.09$	LAF

we used two observation modes—the image-defocus technique between 2004 and 2013, and a technique using the local attenuation filter (LAF) between 2014 and 2016. The LAF was originally developed for the IRSF 1.4 m telescope for the observation of very bright NIR stars (Nagayama 2016), and was also installed on the Kagoshima University 1 m telescope (T. Nagayama et al. in preparation). Tables 4, 5, and 6 show the obtained  $J$ -,  $H$ -, and  $K'$ -band magnitudes for all the observation epochs.

**Table 5.** Near-infrared photometry results of V837 Her.

MJD	$m_J$ (mag)	$m_H$ (mag)	$m_K$ (mag)	Remark
53132	–	$2.15 \pm 0.01$	$1.44 \pm 0.02$	defocus
53279	$3.20 \pm 0.03$	$1.97 \pm 0.02$	$1.23 \pm 0.09$	defocus
53316	$3.38 \pm 0.02$	$2.16 \pm 0.02$	–	defocus
53415	$4.21 \pm 0.02$	–	$2.02 \pm 0.07$	defocus
53495	$4.58 \pm 0.28$	–	–	defocus
54170	–	$2.74 \pm 0.17$	–	defocus
54191	$2.93 \pm 0.02$	$1.77 \pm 0.01$	$1.03 \pm 0.03$	defocus
54912	–	$2.63 \pm 0.03$	$1.77 \pm 0.05$	defocus
54929	$4.14 \pm 0.01$	–	$1.91 \pm 0.03$	defocus
54952	$4.39 \pm 0.02$	$2.91 \pm 0.02$	–	defocus
54971	–	–	$2.08 \pm 0.04$	defocus
54998	$4.33 \pm 0.05$	$2.96 \pm 0.01$	–	defocus
55070	–	$2.70 \pm 0.06$	–	defocus
55119	–	–	$1.74 \pm 0.04$	defocus
55657	–	$2.99 \pm 0.02$	$2.15 \pm 0.07$	defocus
55688	$2.12 \pm 0.04$	–	–	defocus
55985	$3.97 \pm 0.07$	$2.71 \pm 0.06$	$1.87 \pm 0.07$	defocus
56155	–	–	$2.29 \pm 0.03$	defocus
56204	$3.17 \pm 0.02$	–	$1.59 \pm 0.05$	defocus
56763	–	–	$1.22 \pm 0.03$	defocus
56867	–	–	$1.13 \pm 0.06$	LAF
56908	–	–	$1.26 \pm 0.08$	LAF
56910	–	–	$1.24 \pm 0.06$	LAF
56917	–	–	$1.31 \pm 0.07$	LAF
56939	–	–	$1.28 \pm 0.07$	LAF
56958	–	–	$1.53 \pm 0.07$	LAF
56981	–	–	$1.76 \pm 0.06$	LAF
57276	–	–	$1.66 \pm 0.07$	LAF
57332	–	–	$1.30 \pm 0.07$	LAF
57591	–	–	$2.23 \pm 0.08$	LAF
57618	–	–	$2.22 \pm 0.08$	LAF

**Table 6.** Near-infrared photometry results of BX Cam.

MJD	$m_J$ (mag)	$m_H$ (mag)	$m_K$ (mag)	Remark
53243	–	–	$1.20 \pm 0.01$	defocus
53279	–	–	$1.42 \pm 0.09$	defocus
53305	–	–	$1.69 \pm 0.03$	defocus
53326	–	–	$1.85 \pm 0.02$	defocus
53352	–	–	$2.02 \pm 0.02$	defocus
53406	–	–	$1.77 \pm 0.06$	defocus
54159	–	–	$1.88 \pm 0.03$	defocus
54179	–	–	$1.69 \pm 0.06$	defocus
54201	–	–	$1.89 \pm 0.02$	defocus
54228	–	–	$2.03 \pm 0.02$	defocus
54473	–	–	$0.61 \pm 0.05$	defocus
54510	–	–	$0.79 \pm 0.03$	defocus
54524	–	–	$0.72 \pm 0.02$	defocus
54584	–	–	$0.63 \pm 0.08$	defocus
54871	–	–	$0.38 \pm 0.06$	defocus

**Table 7.** Spot list of AP Lyn.\*

ID	$v_{\text{LSR}}$ ( $\text{km s}^{-1}$ )	$\Delta\alpha\cos\delta$ (mas)	$\Delta\delta$ (mas)	$I_{\text{peak}}$ (Jy) beam $^{-1}$
— First epoch 2006 10 28 —				
A	–28.0	$-18.29 \pm 0.01$	$19.90 \pm 0.01$	$6.86 \pm 0.14$
D	–27.6	$-79.75 \pm 0.06$	$35.78 \pm 0.04$	$0.86 \pm 0.09$
C	–14.9	$-93.28 \pm 0.02$	$26.39 \pm 0.02$	$2.02 \pm 0.08$
— Second epoch 2006 11 26 —				
A	–28.0	$-18.92 \pm 0.02$	$18.35 \pm 0.01$	$3.96 \pm 0.12$
C	–14.9	$-94.25 \pm 0.05$	$24.86 \pm 0.04$	$0.94 \pm 0.09$
— Third epoch 2007 01 05 —				
A	–28.0	$-20.02 \pm 0.01$	$16.05 \pm 0.01$	$2.32 \pm 0.05$
B	–28.0	$-15.71 \pm 0.03$	$15.54 \pm 0.02$	$1.29 \pm 0.05$
C	–14.9	$-95.82 \pm 0.04$	$22.67 \pm 0.04$	$0.57 \pm 0.05$
— Fourth epoch 2007 02 09 —				
A	–28.0	$-21.07 \pm 0.02$	$13.47 \pm 0.02$	$1.80 \pm 0.08$
B	–28.0	$-16.76 \pm 0.04$	$12.97 \pm 0.02$	$1.40 \pm 0.08$
C	–14.9	$-97.00 \pm 0.06$	$20.13 \pm 0.07$	$0.50 \pm 0.07$
— Fifth epoch 2007 03 16 —				
A	–28.0	$-21.51 \pm 0.03$	$10.59 \pm 0.02$	$1.49 \pm 0.08$
B	–28.0	$-17.07 \pm 0.03$	$10.05 \pm 0.02$	$1.43 \pm 0.08$
— Sixth epoch 2007 04 08 —				
A	–28.0	$-21.40 \pm 0.02$	$8.56 \pm 0.02$	$1.92 \pm 0.10$
B	–28.0	$-16.96 \pm 0.03$	$8.04 \pm 0.02$	$2.03 \pm 0.10$
— Seventh epoch 2007 05 05 —				
A	–28.0	$-21.00 \pm 0.02$	$6.24 \pm 0.02$	$2.72 \pm 0.12$
B	–28.0	$-16.42 \pm 0.03$	$5.70 \pm 0.02$	$2.88 \pm 0.12$
C	–14.9	$-98.19 \pm 0.10$	$12.99 \pm 0.07$	$0.60 \pm 0.10$
— Eighth epoch 2007 09 08 —				
A	–28.0	$-16.89 \pm 0.02$	$-2.37 \pm 0.01$	$6.19 \pm 0.21$
B	–28.0	$-12.39 \pm 0.02$	$-2.80 \pm 0.01$	$7.62 \pm 0.20$
C	–14.9	$-95.63 \pm 0.06$	$4.54 \pm 0.04$	$1.12 \pm 0.10$
E	–22.9	$-87.50 \pm 0.04$	$10.63 \pm 0.04$	$1.12 \pm 0.09$
F	–18.3	$22.32 \pm 0.02$	$15.67 \pm 0.01$	$3.19 \pm 0.11$
G	–15.8	$-61.10 \pm 0.05$	$-28.40 \pm 0.05$	$0.94 \pm 0.10$
H	–15.4	$-67.53 \pm 0.03$	$9.18 \pm 0.03$	$1.80 \pm 0.10$
I	–14.5	$23.76 \pm 0.04$	$6.13 \pm 0.02$	$1.60 \pm 0.10$

\*Column 1 lists the spot ID. Column 2 lists the local standard of rest (LSR) velocity. Columns 3 and 4 list the RA and Dec offset with respect to the delay tracking center in table 3, respectively. Column 5 lists the peak intensity.

### 3 Results

#### 3.1 Annual parallaxes of AP Lyn and V837 Her

The annual parallaxes are obtained from the positional variation of maser spots. Tables 7 and 8 list the maser spots of AP Lyn and V837 Her detected in individual epochs. The peak position, ( $\Delta\alpha\cos\delta$ ,  $\Delta\delta$ ), and the peak intensity,  $I_{\text{peak}}$ , obtained by AIPS IMFIT are shown in the tables. We detected nine spots in AP Lyn and four spots in V837 Her. Three spots (A, B, and C) for AP Lyn and two spots (A and B) for V837 Her were persistently detected for more than three epochs and used for the parallax



measurement. The phase-referenced images of the representative spots A are shown in figure 2. Their structures seem to be point-like.

The annual parallaxes of AP Lyr and V837 Her were obtained to be  $2.008 \pm 0.038$  mas and  $1.090 \pm 0.014$  mas, respectively. The corresponding distances are  $498 \pm 10$  pc and  $917 \pm 12$  pc. The parallax was obtained by combined fitting using multiple maser spots, in which their positional variations were fitted by the common parallaxes and the

**Table 8.** Spot list of V837 Her.\*

ID	$v_{\text{LSR}}$ ( $\text{km s}^{-1}$ )	$\Delta\alpha\cos\delta$ (mas)	$\Delta\delta$ (mas)	$I_{\text{peak}}$ (Jy $\text{beam}^{-1}$ )
— First epoch 2009 10 25 —				
B	-22.4	$-1.12 \pm 0.07$	$-3.06 \pm 0.08$	$1.60 \pm 0.24$
— Second epoch 2010 01 10 —				
A	-24.1	$0.91 \pm 0.02$	$-5.41 \pm 0.02$	$5.54 \pm 0.23$
B	-22.4	$0.25 \pm 0.02$	$-4.12 \pm 0.02$	$6.94 \pm 0.26$
C	-13.6	$-19.58 \pm 0.07$	$14.67 \pm 0.06$	$1.35 \pm 0.19$
— Third epoch 2010 04 02 —				
A	-24.1	$2.08 \pm 0.01$	$-5.16 \pm 0.01$	$9.82 \pm 0.25$
B	-22.4	$1.31 \pm 0.01$	$-3.95 \pm 0.01$	$15.29 \pm 0.31$
C	-13.6	$-19.11 \pm 0.05$	$15.38 \pm 0.05$	$2.45 \pm 0.19$
— Fourth epoch 2010 11 04 —				
A	-24.1	$0.83 \pm 0.13$	$-7.20 \pm 0.14$	$1.58 \pm 0.22$
— Fifth epoch 2011 01 15 —				
A	-24.1	$2.21 \pm 0.07$	$-8.42 \pm 0.07$	$1.14 \pm 0.18$
D	-12.7	$-14.05 \pm 0.06$	$1.96 \pm 0.05$	$1.82 \pm 0.18$
— Sixth epoch 2011 04 08 —				
A	-24.1	$3.35 \pm 0.05$	$-8.32 \pm 0.11$	$1.99 \pm 0.28$
— Seventh epoch 2011 11 20 —				
A	-24.1	$2.32 \pm 0.03$	$-11.04 \pm 0.04$	$3.26 \pm 0.22$

\*Column 1 lists the spot ID. Column 2 lists the LSR velocity. Columns 3 and 4 list the RA and Dec offset with respect to the delay tracking center in table 3, respectively. Column 5 lists the peak intensity.

individual linear proper motions for individual spots. The fitting results are shown in figure 3. In the plot of time vs. position offset, we can clearly see sinusoidal motion with a period of 1 yr caused by the parallax. The post-fit residuals in the RA and Dec directions are  $(\sigma_\alpha, \sigma_\delta) = (0.075, 0.125)$  mas for AP Lyr and  $(0.024, 0.201)$  mas for V837 Her, respectively.

We compare the parallaxes from VERA and Gaia. The Gaia DR2 catalog reported  $\pi = 1.96 \pm 0.23$  mas and  $\pi = 1.41 \pm 0.25$  mas for the parallaxes of AP Lyr and V837 Her, respectively (Gaia Collaboration 2016, 2018). The VERA and Gaia parallaxes of AP Lyr are consistent within error; however, those of V837 Her had a 29% discrepancy. This difference could be related to the following: (1) our parallaxes are determined with H<sub>2</sub>O masers, which may be associated with outflow due to mass loss and located a small distance from the Mira variable star, and (2) the estimated stellar size of  $\sim 3$  mas is larger than that from the observed Gaia parallax, indicating that measuring the precise position of the star and its positional change is difficult unless the brightness distribution of the star is very simple. This result suggests that VLBI astrometry is still useful for parallax measurements of evolved stars in particular.

The proper motions of the maser spots in AP Lyr and V837 Her are listed in tables 9 and 10, respectively. These proper motions are the sum of the systemic motions and the internal motions of the maser spots. The averages of the proper motions are calculated and their values are shown in the tables. The average LSR velocities of all detected spots are also calculated to be  $-20.6 \pm 1.9$   $\text{km s}^{-1}$  for AP Lyr and  $-18.2 \pm 2.6$   $\text{km s}^{-1}$  for V837 Her. These are consistent with the average LSR velocities of SiO masers of approximately  $-19$   $\text{km s}^{-1}$  for AP Lyr and approximately  $-17$   $\text{km s}^{-1}$  for V837 Her (Kim et al. 2010).

The maser spot distributions of AP Lyr and V837 Her are shown in figure 4. The reference epoch of figure 4,

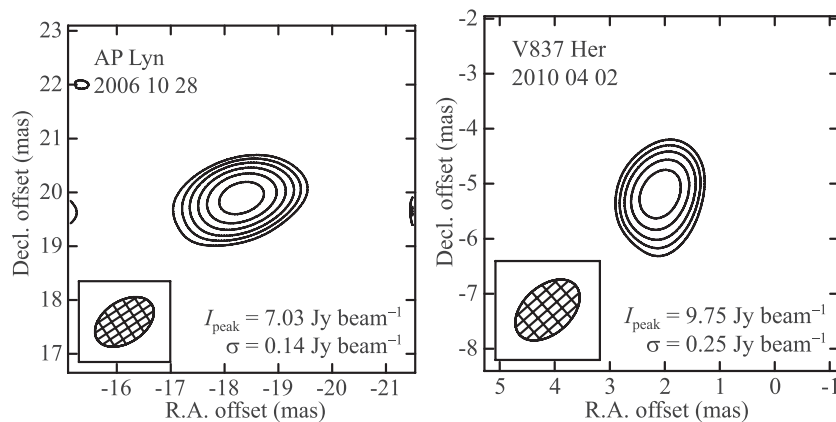


**Fig. 2.** Phase-referenced maps of the H<sub>2</sub>O maser spots at  $v_{\text{LSR}} = -28.0$   $\text{km s}^{-1}$  in AP Lyr (left) and  $v_{\text{LSR}} = -24.1$   $\text{km s}^{-1}$  in V837 Her (right). The peak intensity ( $I_{\text{peak}}$ ) and the noise level ( $\sigma$ ) are shown in the bottom corner. The contour levels are  $\sigma \times 5 \times \sqrt{2^n}$  ( $n = 1, 2, 3, \dots$ ).

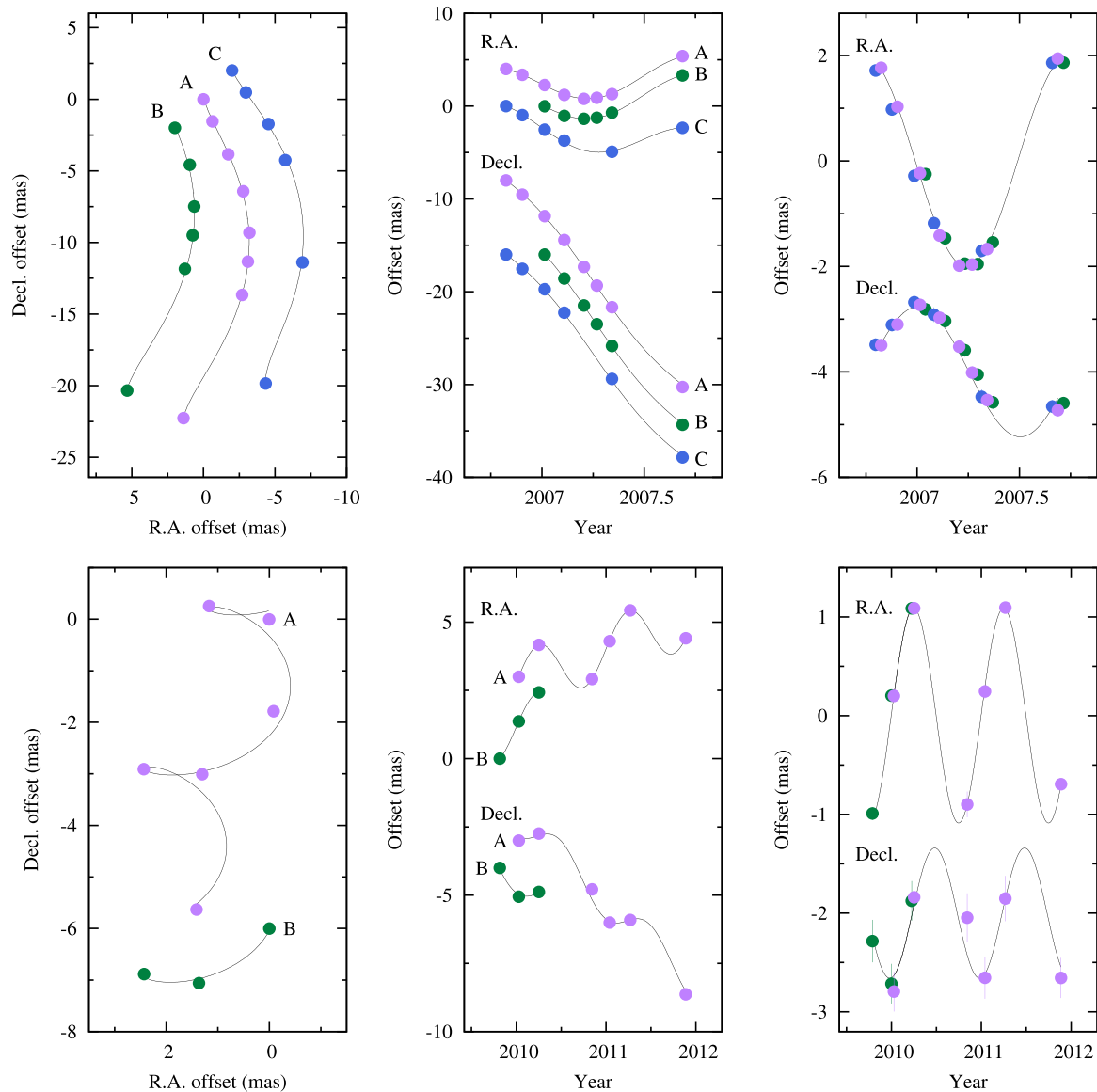


**Fig. 3.** Parallaxes and proper motions of AP Lyn (top three panels) and V837 Her (bottom three panels). The solid line shows the best-fitting results for parallax and proper motion. Left: Positions on the sky. Middle: RA and Dec offset versus time. Right: As the middle panel, except the proper motion has been removed, allowing the effect of only the parallax to be seen. A, B, and C in the middle panels represent maser feature IDs.

table 9, and table 10 is the eighth epoch (2007/09/08) for AP Lyn and the third epoch (2010/04/02) for V837 Her. For AP Lyn, spot D was only detected in the first epoch. Its position in the eighth epoch was estimated using the position offset with respect to spot A, which was detected in both epochs. Similarly, for V837 Her, spot D was detected in only the fifth epoch. Its position in the third epoch was estimated using the position offset with respect to spot A. The maser spots of AP Lyn are distributed in an area of  $120 \text{ mas} \times 50 \text{ mas}$  ( $60 \text{ au} \times 25 \text{ au}$ ). The red-shifted spot and the blue-shifted spots are expanded in the west–east direction with a velocity of  $\sim 2 \text{ mas yr}^{-1}$  ( $5 \text{ km s}^{-1}$ ). The red-shifted spot and the blue-shifted spots

are separated by  $\sim 30 \text{ mas}$  ( $28 \text{ au}$ ) in V837 Her, and they expanded in the northwest–southeast direction with a velocity of  $\sim 2 \text{ mas yr}^{-1}$  ( $9 \text{ km s}^{-1}$ ). Another red-shifted spot is detected near the central star.

### 3.2 Infrared light curves of AP Lyn, V837 Her, and BX Cam

The results of our infrared photometric monitoring observations using the Kagoshima 1 m telescope are presented in Figures 5, 6, and 7 for AP Lyn, V837 Her, and BX Cam, respectively. Using  $J$ -,  $H$ -, and  $K'$ -band data ( $K'$ -band only

**Table 9.** Spot list of AP Lyn.\*

ID	$\Delta\alpha\cos\delta$ (mas)	$\Delta\delta$ (mas)	$\mu_\alpha\cos\delta$ (mas yr <sup>-1</sup> )	$\mu_\delta$ (mas yr <sup>-1</sup> )	$v_{\text{LSR}}$ (km s <sup>-1</sup> )
A	-16.89 ± 0.02	-2.37 ± 0.01	1.42 ± 0.09	-24.39 ± 0.16	-28.0
B	-12.39 ± 0.02	-2.80 ± 0.01	1.79 ± 0.13	-24.59 ± 0.22	-28.0
C	-95.63 ± 0.06	4.54 ± 0.04	-2.89 ± 0.12	-23.98 ± 0.17	-14.9
D	-78.35 ± 0.06	13.51 ± 0.04	-	-	-27.6
E	-87.50 ± 0.04	10.63 ± 0.04	-	-	-22.9
F	22.32 ± 0.02	15.67 ± 0.01	-	-	-18.3
G	-61.10 ± 0.05	-28.40 ± 0.05	-	-	-15.8
H	-61.53 ± 0.03	9.18 ± 0.03	-	-	-15.4
I	23.76 ± 0.04	6.13 ± 0.02	-	-	-14.5
Mean			0.11 ± 1.23	-24.32 ± 0.15	-20.6 ± 1.9

\*Column 1 lists the spot ID. Columns 2 and 3 list the RA and Dec offset with respect to the delay tracking center in table 3 at 2007 September 08, respectively. Columns 4 and 5 list the proper motions in the RA and Dec directions, respectively. Column 6 lists the LSR velocity.

**Table 10.** Spot list of V837 Her.\*

ID	$\Delta\alpha\cos\delta$ (mas)	$\Delta\delta$ (mas)	$\mu_\alpha\cos\delta$ (mas yr <sup>-1</sup> )	$\mu_\delta$ (mas yr <sup>-1</sup> )	$v_{\text{LSR}}$ (km s <sup>-1</sup> )
A	2.08 ± 0.01	-5.16 ± 0.01	1.24 ± 0.01	-3.10 ± 0.09	-24.1
B	1.31 ± 0.01	-3.95 ± 0.01	0.81 ± 0.05	-2.96 ± 0.46	-22.4
C	-19.11 ± 0.05	15.38 ± 0.14	-1.84 ± 0.24	-0.01 ± 0.88	-13.6
D	-14.18 ± 0.06	5.22 ± 0.05	-	-	-12.7
Mean			0.07 ± 0.78	-2.03 ± 0.82	-18.2 ± 2.6

\*Column 1 lists the spot ID. Columns 2 and 3 list the RA and Dec offset with respect to the delay tracking center in table 3 at 2010 April 2, respectively. Columns 4 and 5 list the proper motions in the RA and Dec directions, respectively. Column 6 lists the LSR velocity.

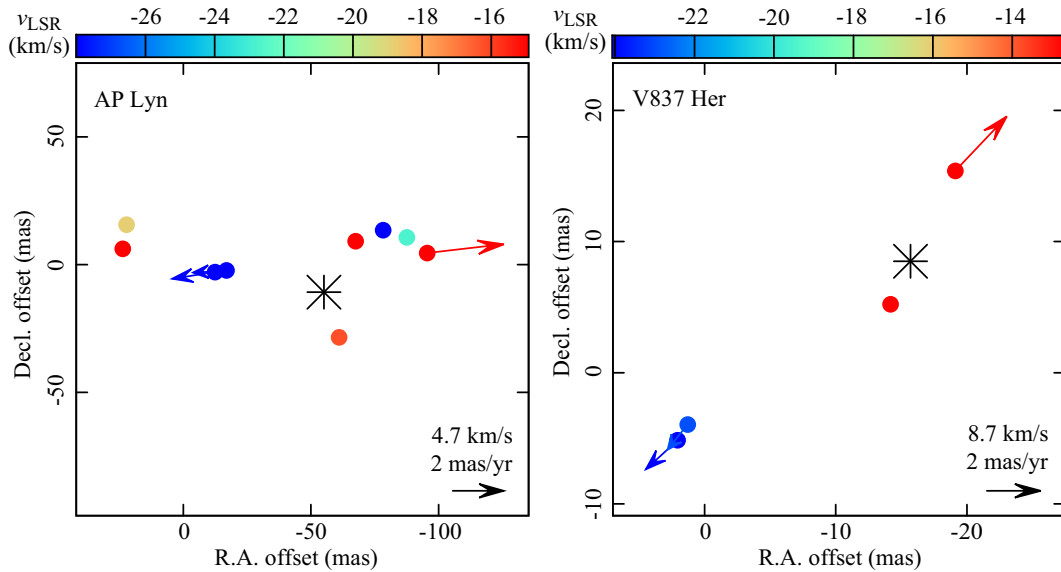


**Fig. 4.** H<sub>2</sub>O maser maps of AP Lyn and V837 Her. The origin (0,0) mas is the coordinate shown in table 3. The asterisk shows the stellar position estimated by Gaia DR2 (Gaia Collaboration 2018).

in the case of BX Cam), we solved for the period  $P$  by assuming a sinusoidal function,

$$m = m_0 + A \sin[2\pi(t + \theta)/P], \quad (1)$$

where  $m$  is the apparent magnitude,  $m_0$  is the averaged magnitude,  $A$  is the amplitude, and  $\theta$  is the voluntary phase. We fitted the trigonometric function to the light curves of AP Lyn, V837 Her, and BX Cam (see Urigo et al. 2020).



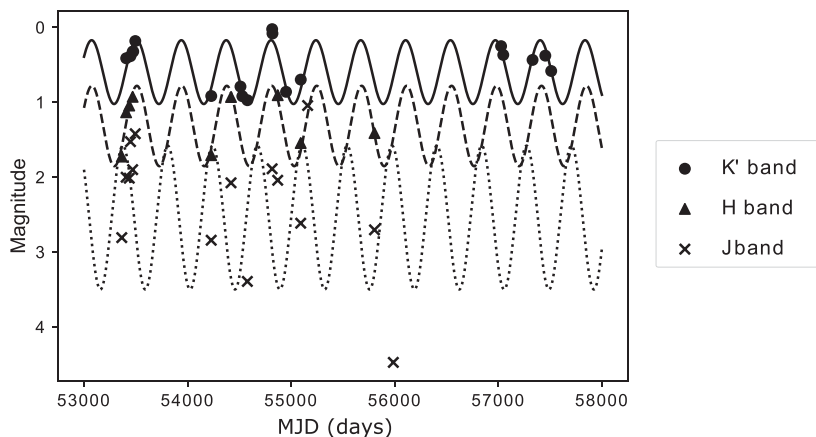


**Fig. 5.** Infrared  $J$ -,  $H$ -,  $K'$ -band light curves of AP Lyn. The crosses, filled triangles, and filled circles represent the  $J$ ,  $H$ , and  $K'$  bands, respectively. The solid lines represent the  $K'$ -band light curve, the dashed lines the  $H$ -band light curve, and the dotted lines the  $J$ -band light curve. The period fitted with the  $K'$ -band data is 433 d.

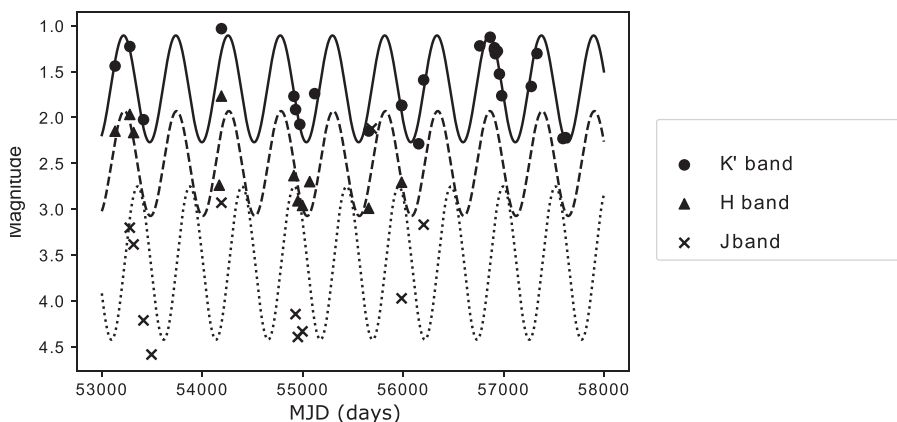


**Fig. 6.** Infrared  $J$ -,  $H$ -, and  $K'$ -band light curves of V837 Her. The crosses, filled triangles, and filled circles represent the  $J$ ,  $H$ , and  $K'$  bands, respectively. The solid lines represent the  $K'$ -band light curve, the dashed lines the  $H$ -band light curve, and the dotted lines the  $J$ -band light curve. The period fitted with the  $K'$ -band data is 520 d.

Since Mira variables often show several periods, we present the fitting results with local minimum root-mean-square (RMS) in the limited time span. We derived the period ( $K'$ -band data only), mean magnitude, and the amplitudes in each band for AP Lyn, V837 Her, and BX Cam. The mean magnitudes and amplitudes in the  $J$  and  $H$  bands were derived using the period obtained from the  $K'$ -band data. The period of BX Cam was derived using a combination of our  $K'$ -band data and those of Jones et al. (1990) to increase the number of detected cycles.

The derived  $K'$ -band periods were  $433 \pm 1$  d for AP Lyn,  $520 \pm 2$  d for V837 Her, and  $458 \pm 1$  d for BX Cam. The errors were derived from least-squares fitting. The other parameters are shown in tables 11, 12, and 13. The American Association of Variable Star Observers (AAVSO) has 442 d, 514 d, and 440 d as the periods of AP Lyn, V837 Her, and BX Cam, respectively.

## 4 Discussion

### 4.1 Photometric properties of AP Lyn, V837 Her, and BX Cam

Exploring the physical photometric properties of V837 Her, AP Lyn, and BX Cam, we have derived the absolute bolometric magnitude ( $M_{\text{bol}}$ ), luminosity ( $L$ ), effective temperature ( $T_{\text{eff}}$ ), and radius ( $R$ ) for each target. First, we determine the  $V - K$  values, and use them to estimate  $T_{\text{eff}}$  and  $BC_K$  from effective temperature versus  $V - K$  and  $BC_K$  versus  $V - K$  diagrams, as shown in Buzzoni et al. (2010).

#### 4.1.1 V837 Her

With the average  $V$ -band magnitude of V837 Her obtained from the International Variable Star Index (VSX)<sup>1</sup> and the  $K$ -band magnitude from our NIR observations, we

<sup>1</sup> (<https://www.aavso.org/vsx/>).

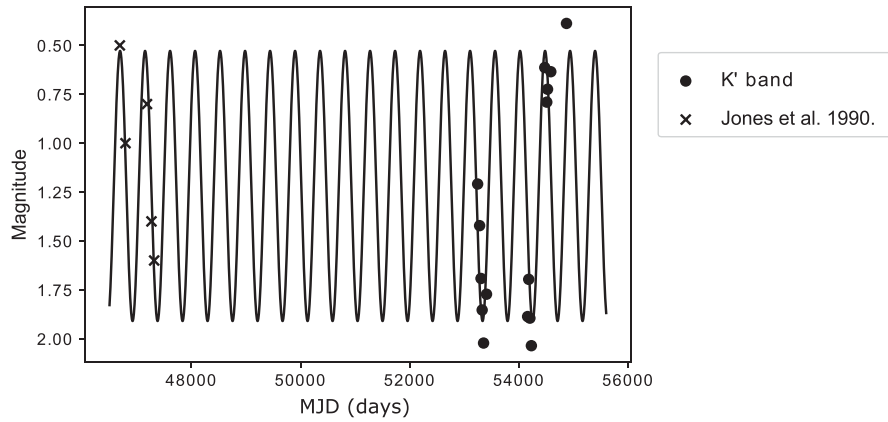


**Fig. 7.** Infrared  $K'$ -band light curves of BX Cam. The filled circles are the data from our observations, while the crosses represent data points taken from Jones et al. (1990). The solid lines represent the  $K'$ -band light curve. The period fitted with the  $K'$ -band data is 458 d.

**Table 11.** Results of fitting AP Lyn.

Filter	Period [d]	Mean magnitude [mag]	Amplitude [mag]
$J$	433	$2.55 \pm 0.12$	0.78
$H$	433	$1.32 \pm 0.03$	0.50
$K'$	433	$0.60 \pm 0.01$	0.40

**Table 12.** Results of fitting V837 Her.

Filter	Period [d]	Mean magnitude [mag]	Amplitude [mag]
$J$	520	$3.47 \pm 0.08$	0.83
$H$	520	$2.35 \pm 0.04$	0.67
$K'$	520	$1.68 \pm 0.03$	0.64

**Table 13.** Results of fitting BX Cam.

Filter	Period [d]	Mean magnitude [mag]	Amplitude [mag]
$K'$	458	$1.21 \pm 0.11$	0.69

obtained  $V - K$  of  $11.62 \pm 0.66$  mag. Based on Buzzoni et al. (2010), the  $T_{\text{eff}}$  and  $BC_K$  of V837 Her will correspond to  $3157 \pm 209$  K and  $3.22 \pm 0.18$  mag, respectively. The bolometric magnitude ( $m_{\text{bol}}$ ) of V837 Her can be computed from  $BC_K$  using  $m_{\text{bol}} = BC_K + m_K$ ; we obtained an  $m_{\text{bol}}$  of  $4.90 \pm 0.19$  mag. The absolute bolometric magnitude ( $M_{\text{bol}}$ ) of V837 Her can be computed from  $m_{\text{bol}}$  using  $M_{\text{bol}} = m_{\text{bol}} - 5 \cdot \log_{10}(D/10)$ , where  $D$  is the distance to the source; we obtained  $M_{\text{bol}} = -4.95 \pm 0.27$  mag. To derive the radius of V837 Her, we used the relation  $M_{\text{bol}} = 4.74 - 2.5 \cdot \log[T_{\text{eff}}^4 \cdot R^2 / (T_{\text{eff}\odot}^2 \cdot R_{\odot}^2)]$  (Bessell et al. 1998) and obtained a radius of  $291 \pm 35 R_{\odot}$ .

#### 4.1.2 AP Lyn

With a mean  $V$ -band magnitude of AP Lyn of 12.8 mag obtained from VSX<sup>1</sup> and the  $K$ -band magnitude from our NIR observations, we obtained a  $V - K$  of  $12.20 \pm 0.32$  mag. We derived the properties of AP Lyn the same way as above, and  $T_{\text{eff}}$  and  $BC_K$  of AP Lyn correspond to  $3141 \pm 200$  K and  $3.24 \pm 0.18$  mag, respectively. The bolometric magnitude ( $m_{\text{bol}}$ ) of AP Lyn can be computed to be  $3.84 \pm 0.18$  mag, from which we obtained  $M_{\text{bol}} = -4.60 \pm 0.45$  mag. The radius is derived to be  $R = 250 \pm 24 R_{\odot}$ .

#### 4.1.3 BX Cam

With the average  $V - K$  of  $14.09 \pm 0.66$  mag,  $T_{\text{eff}}$  and  $BC_K$  correspond to  $3100 \pm 209$  K and  $3.28 \pm 0.18$  mag, respectively. The bolometric magnitude is computed to be  $m_{\text{bol}} = 4.18 \pm 0.15$  mag, and the absolute bolometric magnitude to be  $M_{\text{bol}} = 4.59 \pm 0.27$  mag with a distance of  $D = 0.58$  kpc (Matsuno et al. 2020). The radius is derived to be  $R = 256 \pm 35 R_{\odot}$ .

#### 4.1.4 Initial masses

We find the absolute luminosities at  $\log(L_{\text{obs}}/L_{\odot}) = 3.73 \pm 0.18$ ,  $3.88 \pm 0.11$ , and  $3.52 \pm 0.11$ , respectively, for AP Lyn, V837 Her, and BX Cam. These values are in a similar range to OZ Gem [ $\log(L_{\text{obs}}/L_{\odot}) = 3.76 \pm 0.10$ ]. From the observed luminosity, we may evaluate the initial masses of these stars through a comparison with the evolutionary models of AGB stars. Figure 8 shows the luminosity at the stage when the star evolves to the beginning of the major thermal pulse (TP-AGB phase) as a function of the initial mass,  $M_i$ , at the zero-age main sequence, taken from the computations for the solar metallicity by Lattanzio (1986). We can read off the initial masses at which the stars just reach the TP-AGB phase with the observed luminosity in the range  $3.3 \leq \log(L_{\text{obs}}/L_{\odot}) \leq 3.9$ . Thus, the situation is same as OZ Gem, considered by Urigo et al. (2020b).

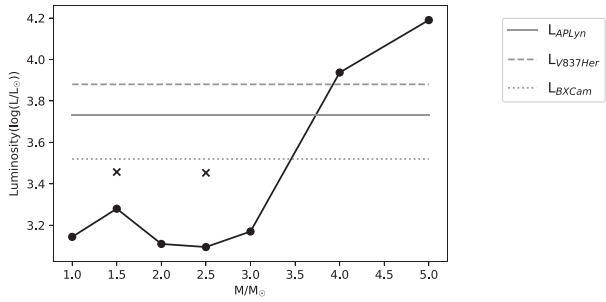


**Fig. 8.** Initial mass–luminosity diagram of AGB stars, derived from table 8 of Lattanzio (1986) for a helium abundance of  $Y = 0.2$  (black dots and solid line) and  $Y = 0.3$  (crosses). The horizontal axis is the initial mass,  $M_i$ , at the zero-age main sequence, taken from the computations for solar metallicity by Lattanzio (1986). The luminosities derived for AP Lyn, V837 Her, and BX Cam are also plotted as gray solid, dashed, and dotted lines, respectively.

There are two possible ranges of initial mass for which a star can retain an O-rich surface until it attains the observed luminosity. One is the low-mass range of  $M_i < M_{\text{TDU},\text{min}}$ , where  $M_{\text{TDU},\text{min}}$  is the lower limit of the stellar mass with which the star undergoes TDU during the TP-AGB phase; a star with initial mass in this range gets through the TP-AGB phase without suffering from TDUs and the resultant change in the surface chemistry. The lower mass limit for TDU to occur is estimated at  $1.5 M_{\odot} \leq M_{\text{TDU},\text{min}} \leq 2.2 M_{\odot}$  for solar metallicity ( $Z = 0.02$ ), though this is subject to uncertainties, particularly in the prescription for the convective mixing, and is dependent on the metallicity (Lattanzio 1986; Karakas 2010). The other is the high-mass range of  $M_i \geq M_{\text{TP}}(L_{\text{obs}})$ ; in this range, the star stays in the early AGB (E-AGB) phase before entering the TP-AGB phase and the surface abundance is left untouched. For initial masses in the range  $M_{\text{TDU},\text{min}} < M_i < M_{\text{TP}}(L_{\text{obs}})$ , the stars are deemed to have started the TP-AGB phase with TDU and developed C-rich surface abundances by the time of reaching the observed luminosity. In addition, we may well consider that the luminosity of the sample stars are too low for hot bottom burning to play a part in the surface chemistry, as argued for some O-rich Miras in the LMC. As a consequence, our result is indicative that the four stars all belong to the low-mass range where stars end their TP-AGB evolution keeping an O-rich abundance in the envelope.

#### 4.2 Period–magnitude diagram (period–luminosity relation)

Figure 9 shows the locations of our three samples (AP Lyn, V837 Her, and BX Cam), as well as the Galactic long-period Mira variable star OZ Gem (Urago et al. 2020b), on the period–absolute magnitude ( $M_K$ – $\log P$ ) diagram for LMC

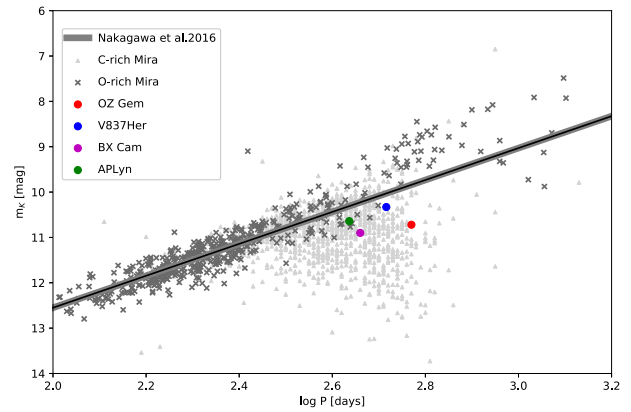


**Fig. 9.** Locations of AP Lyn and V837 Her (black filled squares) are compared with that of OZ Gem (red filled circle) on the period–magnitude diagram of Mira variables of the LMC (triangles and crosses denote C-rich and O-rich Miras, respectively). The thick solid line shows the  $P$ – $L$  relation of Galactic Miras from Nakagawa et al. (2016).

stars. OZ Gem also has a high mass-loss rate and has formed a thick circumstellar dust envelope. It is shown for comparison because it is an OH/IR star shown on the period–luminosity diagram with a tendency to be dimmed by circumstellar dust. Our O-rich Miras fall in the area occupied by C-rich Miras in the LMC. O-rich Miras in the LMC are distributed mostly in the short periods of  $\log P(\text{days}) \lesssim -2.4$ , and for larger periods, gradually replaced by C-rich Miras, which grow sparse beyond  $\log P \simeq 2.8$ . On the other hand, O-rich Miras with long periods form a distribution with a slightly steeper slope for  $\log P \gtrsim 2.5$  and extending beyond  $\log P = 3$ ; these stars are attributed to TP-AGB stars with larger initial mass and experiencing TDUs and hot bottom burning. We plot the regression line derived by Nakagawa et al. (2016) for Galactic O-rich Miras with measured parallaxes mostly of  $\log P \lesssim 2.6$  and assuming the same slope as Ita et al. (2004) obtained from LPVs in the LMC. It is argued that the metallicity has little effect on the period–magnitude relation for O-rich Miras of short periods ( $P < 350$  d) between the Galaxy and the LMC (e.g., Matsunaga 2012). Our three stars and OZ Gem, with periods of  $\log P > 2.6$ , are all situated below the line and tend to be darker than extrapolated from Miras of short periods, similarly to C-rich Miras in the LMC. The dimming tendency is obvious from the NIR color–color diagram in figure 10. They suffer more reddening than most O-rich Miras and lie on the same strip dominated by C-rich Miras, though the degrees are smaller, which is evidence of obscuration by circumstellar dust shells.

In fact, Utenthaler et al. (2019) reported AP Lyn and BX Cam to be losing mass at  $\dot{M}_{\text{loss}} \sim 7 \times 10^{-6} M_{\odot} \text{ yr}^{-1}$ , which is comparable to OZ Gem’s mass loss. These mass loss rates considerably exceed the growth rates of the core,  $\dot{M}_{\text{nuc}} \equiv L_{\text{obs}}/(X_{\text{env}} E_{\text{H}}) =$

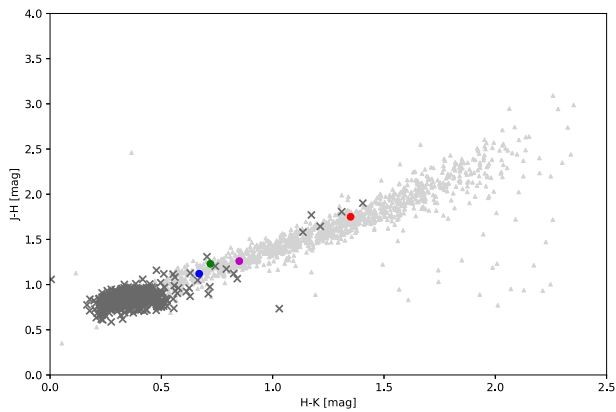


**Fig. 10.** Near-infrared color-color diagram of V837 Herand AP Lyn (black filled squares) in comparison with OZ Gem (black filled circle) and C-rich (triangles) and O-rich Miras (crosses) in the LMC.

$1.5 \times 10^{-7} (L/5000L_{\odot}) M_{\odot} \text{ yr}^{-1}$ , where  $X_{\text{env}}$  and  $E_{\text{H}}$  are the hydrogen concentration in the envelope and the energy release from a unit mass of hydrogen, respectively. This indicates that these stars will end their lives as O-rich Miras before increasing their luminosity and pulsation period appreciably. Some O-rich Miras in the LMC show similar reddening to our samples, though with large periods, in particular  $\log P \simeq 3$  for those near to OZ Gem. The luminosity of TP-AGB stars is correlated with the core mass, which may vary with the metallicity, though slightly, through the dependence of the hydrogen shell burning rate on the CNO and He abundances (e.g., Fujimoto et al. 1995). The pulsation periods of TP-AGB stars, especially of the fundamental mode, are scaled by  $P \propto [G(M - M_{\text{c}})/R^3]^{1/2}$ , where  $M$  and  $M_{\text{c}}$  are the current stellar mass and core mass, and hence are little dependent on the metallicity (e.g., Trabucchi et al. 2019). Accordingly we have to seek counterparts to our sample O-rich stars with similar low initial masses among C-rich stars in the LMC. The difference in the surface chemistry arises from the metallicity dependence of the minimum stellar mass,  $M_{\text{TDU,min}}$ . The numerical models show that  $M_{\text{TDU,min}}$  can be larger for larger metallicity (e.g., Karakas 2014). Larger CNO and helium abundances in the envelope raise the hydrogen burning rate and enlarge the compression rate of the core, which in turn heats up the helium zone to ignite a helium flash with the smaller mass in the helium zone. Since the temperature dependence of helium ignition is strong, the latter prevents the surface convection reaching and dredging up the helium zone for larger metallicity. In the LMC, whose metallicity is lower than the Milky Way,  $M_{\text{TDU,min}}$  can be sufficiently smaller than stars of low mass also experience the dredge-up of carbon via TDU during the TP-AGB phase and readily evolve to be C-rich because of a smaller initial abundance of oxygen, differently from the low-mass stars in the Galaxy. In

contrast, if there are the low-mass stars that get through the TP-AGB phase without TDU in the LMC, they have to expand beyond the pulsation periods observed for our sample stars in the Galaxy because of smaller opacity, but no such correspondences are found among Miras in the LMC. On the other hand, for  $M_{\text{i}} > M_{\text{TP}}$ , the observed periods may mean that the stars have lost a significant fraction of their initial mass, but this is no longer possible because of small observed luminosities, and hence high effective temperatures.

Our sample O-rich Miras are evolved from the AGB stars in the low-mass end. These stars have pulsation periods of  $2.6 \leq \log P \leq 2.7$  and represent OH/IR sources with relatively short periods in the Galaxy, in contrast to OH/IR sources with longer periods of  $\log P > 3$  (Jiménez-Esteban et al. 2006). The latter sources are also observed in the LMC and have a different origin, which is attributed to hot bottom burning in stars of larger initial masses of  $M > 4M_{\odot}$  (e.g., Ventura et al. 2015).

## 5 Conclusions and summary

We have presented VERA observational results of the annual parallaxes of AP Lyn and V837 Her, which were obtained to be  $2.008 \pm 0.038$  mas and  $1.090 \pm 0.014$  mas, corresponding to distances of  $498 \pm 10$  pc and  $917 \pm 12$  pc, respectively. From our infrared observations, we derived the pulsation periods of AP Lyn, V837 Her, and BX Cam to be 433, 520, and 450 d, respectively, using  $K'$ -band light curves.

With the most accurate distance at our disposal, we explored the period-magnitude/luminosity relations of the three sources and confirmed them to be dimming, as in the case of OZ Gem, from the trend of O-rich stars in the LMC. This could be attributed to the metallicity of the Milky Way.

## References

- Bessell, M. S., Castelli, F., & Plez, B. 1998, *A&A*, 333, 231
- Buzzoni, A., Patelli, L., Bellazzini, M., Pecci, F. F., & Oliva, E. 2010, *MNRAS*, 403, 1592
- Celis, L. 1995, *ApJS*, 98, 701
- Engels, D., & Bunzel, F. 2015, *A&A*, 582, A68
- Engels, D., Kreysa, E., Schultz, G. V., & Sherwood, W. A. 1983, *A&A*, 124, 123
- Feast, M. W., Glass, I. S., Whitelock, P. A., & Catchpole, R. M. 1989, *MNRAS*, 241, 375
- Fey, A. L., et al. 2004, *AJ*, 127, 3587
- Fujimoto, M. Y., Sugiyama, K., Iben, I., Jr, & Hollowell, D. 1995, *ApJ*, 444, 175
- Gaia Collaboration, 2016, *A&A*, 595, A1
- Gaia Collaboration, 2018, *A&A*, 616, A1
- Goldman, S. R., et al. 2018, *MNRAS*, 473, 3835
- Honma, M., et al. 2008a, *PASJ*, 60, 935

- Honma, M., Tamura, Y., & Reid, M. J. 2008b, PASJ, 60, 951
- Ita, Y., et al. 2004, MNRAS, 347, 720
- Ita, Y., & Matsunaga, N. 2011, MNRAS, 412, 2345
- Jiménez-Esteban, F. M., García-Lario, P., Engels, D., & Manchado, A. 2006, A&A, 458, 533
- Jones, T. J., Bryja, C. O., Gehrz, R. D., Harrison, T. E., Johnson, J. J., Klebe, D. I., & Lawrence, G. F. 1990, ApJS, 74, 785
- Karakas, A. I. 2010, MNRAS, 403, 1425
- Karakas, A. I. 2014, MNRAS, 445, 347
- Kim, J., Cho, S.-H., & Kim, S. J. 2014, AJ, 147, 22
- Kim, J., Cho, S.-H., Oh, C. S., & Byun, D.-Y. 2010, ApJS, 188, 209
- Knapp, G. R., Pourbaix, D., Platais, I., & Jorissen, A. 2003, A&A, 403, 993
- Lattanzio, J. C. 1986, ApJ, 311, 708
- Luck, R. E., Moffett, T. J., Barnes, T. G., & Gieren, W. P. 1998, AJ, 115, 605
- Matsunaga, N. 2012, Ap&SS, 341, 93
- Matsuno, M., et al. 2020, PASJ, 72, 56
- Nagayama, T. 2016, SPIE Proc., 9912, 991237
- Nakagawa, A., Kurayama, T., Matsui, M., Omodaka, T., Honma, M., Shibata, K. M., Sato, K., & Jike, T. 2016, PASJ, 68, 78
- Orienti, M., Dallacasa, D., Tinti, S., & Stanghellini, C. 2006, A&A, 450, 959
- Stephenson, C. B. 1986, ApJ, 301, 927
- Trabucchi, M., Wood, P. R., Montalbán, J., Marigo, P., Pastorelli, G., & Girardi, L. 2019, MNRAS, 482, 929
- Urago, R., et al. 2020, PASJ, 72, 57
- Urago, R., Omodaka, T., Nagayama, T., Watabe, Y., Miyanosita, R., Matsunaga, N., & Burns, R. A. 2020, ApJ, 891, 50
- Uttenthaler, S., McDonald, I., Bernhard, K., Cristallo, S., & Gobrecht, D. 2019, A&A, 622, A120
- Ventura, P., Karakas, A. I., Dell'Agli, F., Boyer, M. L., García-Hernández, D. A., Di Criscienzo, M., & Schneider, R. 2015, MNRAS, 450, 3181
- Vogt, S. S. 1973, AJ, 78, 389
- Whitelock, P., Marang, F., & Feast, M. 2000, MNRAS, 319, 728
- Yuasa, M., Unno, W., & Magono, S. 1999, PASJ, 51, 197